

## Recirculation of Canada Basin Deep Water in the Amundsen Basin, Arctic

SALAR KARAM<sup>a</sup>, CÉLINE HEUZÉ<sup>a</sup>, VASCO MÜLLER<sup>b</sup>, AND YIXI ZHENG<sup>c</sup>

<sup>a</sup> *Department of Earth Sciences, University of Gothenburg, Gothenburg, Sweden*

<sup>b</sup> *Alfred-Wegener-Institut, Helmholtz-Zentrum für Polar- und Meeresforschung, Bremerhaven, Germany*

<sup>c</sup> *Centre for Ocean and Atmospheric Sciences, School of Environmental Sciences, University of East Anglia, Norwich, United Kingdom*

(Manuscript received 7 December 2022, in final form 2 August 2023, accepted 21 August 2023)

**ABSTRACT:** It is evident from hydrographic profiles in the Arctic Ocean that relatively warm and salty Canada Basin Deep Water (CBDW) flows over the Lomonosov Ridge into the Amundsen Basin, in the Eurasian Arctic. However, oceanographic data in the deep Arctic Ocean are scarce, making it difficult to analyze the spatial extent or the dynamics of this inflow. Here we present new hydrographic data from two recent expeditions as well as historical data from previous expeditions in the central Arctic. We use an end-member analysis to quantify the presence of CBDW in the Amundsen and Nansen Basins and infer new circulation pathways. We find that the inflow of CBDW is intermittent, and that it recirculates in the Amundsen Basin along the Gakkel Ridge. Although the forcing mechanisms for the inflow of CBDW into the Amundsen Basin remain unclear owing to the lack of continuous observations, we demonstrate that density-driven overflows, even intermittent, and the pressure gradient across the Lomonosov Ridge are unlikely drivers. We also find multiple deep eddies with a CBDW content of up to  $600 \text{ g kg}^{-1}$  and a vertical extent of up to 1200 m in the Amundsen Basin. The high CBDW content of these eddies suggests that they can efficiently trap CBDW and transport its heat and salt over long distances.

**KEYWORDS:** Ocean; Arctic; Boundary currents; Eddies; Intermediate waters; Water masses/storage

### 1. Introduction


The Arctic Ocean is split between the Eurasian and Amerasian Basins, with depths exceeding 4000 m, that are separated by the 500–2000-m-deep Lomonosov Ridge (Fig. 1). Although the existence of deep Arctic basins has been established since the Fram expedition (Nansen 1907), the circulation of the various deep-water masses remains largely unknown, in part due to the scarcity of measurements in the deep ice-covered ocean. In particular, little is known about the exchanges of deep water between the two basins, which could play an important role in modifying the properties of the deep ocean.

The water masses of the Arctic Ocean are traditionally separated between the cold and fresh polar mixed layer (different names depending on region and season) from the surface down to a halocline at around a 200-m depth at most; the warm and salty Atlantic layer down to  $\sim 800$  m; the colder Upper Polar Deep Water (UPDW) until  $\sim 1700$  m; and then the deep waters, with different properties, depending on the basin (e.g., Langehaug and Falck 2012). The deep waters of the Amerasian Basin—which should ideally be renamed AABDW, but which we refer to as Canada Basin Deep Water (CBDW) in this study for consistency with previous literature (e.g., Rudels 1986)—are warmer, saltier, and less dense than those of the Eurasian Basin, or Eurasian Basin Deep Water (EBDW) (e.g., Swift et al. 1997). Besides, while the waters of

the Eurasian Basin can communicate with the Nordic seas through the 2500-m deep Fram Strait, the Lomonosov Ridge acts as a topographic barrier. Combined with low or even no new formation of CBDW (Timmermans et al. 2003), this effectively isolates the deep waters of the Amerasian Basin from the global ocean, resulting in a water mass age of 500 years (Schlosser et al. 1997; Tanhua et al. 2009). The relative isolation of CBDW compared to EBDW results in different chemical properties, notably a lower oxygen content (Björk et al. 2010). Although the Lomonosov Ridge inhibits exchanges between the Eurasian and Amerasian Basins, CBDW was detected in the Eurasian Basin during several expeditions (e.g., Björk et al. 2010; Rudels 2012) and was identified notably by Anderson et al. (1994), Jones et al. (1995), and Rudels (1995).

While the inflow of CBDW across the Lomonosov Ridge has been clearly demonstrated, with the main inflow likely occurring via the comparatively deep Intra Basin (e.g., Björk et al. 2007, 2010), there is to date no inventory of CBDW in the Eurasian Basin. Therefore, we currently lack an understanding of the dynamics of the inflow of CBDW and how it circulates in the Arctic Ocean. The recent warming and salinification of the intermediate-depth Atlantic Water (Tsubouchi et al. 2021; Muilwijk et al. 2018; Walczowski et al. 2012) have also been observed in the deep ocean (e.g., Marnela et al. 2016), suggesting a need to better understand the role of the deep ocean in a changing Arctic.

In this study, we present new hydrographic observations from two recent expeditions in the central Arctic Ocean: the Multidisciplinary drifting Observatory for the Study of Arctic Climate (MOSAiC, 2019/20) and the Synoptic Arctic Survey (SAS, 2021), as well as historical measurements. We use an end-member analysis (e.g., Mamayev 1975; Jenkins 1999) to quantify the presence of CBDW in the Amundsen Basin and

 Denotes content that is immediately available upon publication as open access.

Corresponding author: Salar Karam, salar.karam@gu.se

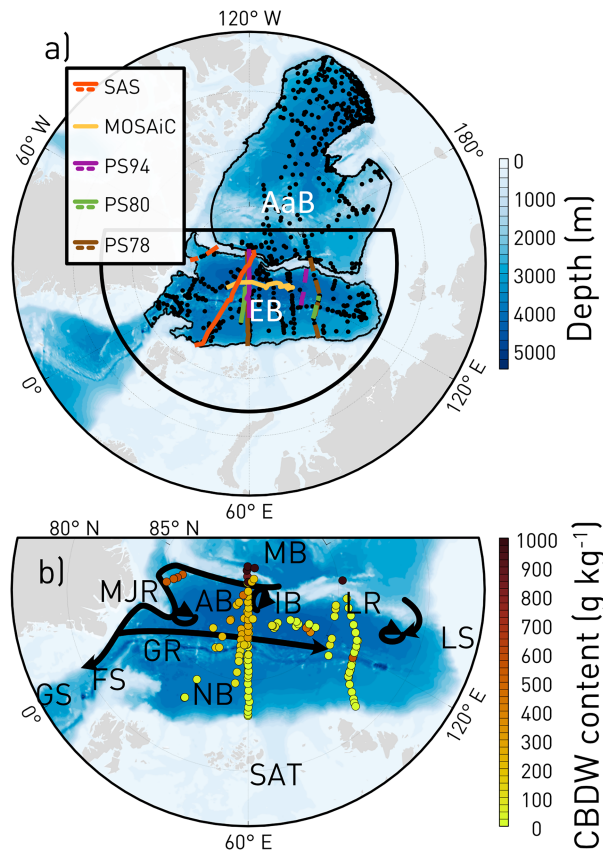


FIG. 1. Stereographic projection showing the bathymetry of the Arctic Ocean (blue–white color scale), from IBCAO (Jakobsson et al. 2020). (a) Location of the hydrographic profiles. The colored lines show the locations of the individual transects analyzed in this study. The small black dots show the locations of all hydrographic profiles used to calculate the properties of the water masses UPDW, CBDW, and EBDW (see Fig. 2 and Table 1). The black contours show the boundaries of the Eurasian Basin (EB) and Amerasian Basin (AaB). The black semicircle shows the inset shown on the bottom panel. (b) Maximum CBDW content found between 1700- and 2000-m depth for each profile (brown–yellow color scale). The black arrows show the inferred circulation pathways of CBDW in the Eurasian Basin and the circling arrows show likely sites of eddy formation for CBDW. It should be noted that none of our transects contain data from the Intra Basin, the suspected main inflow of CBDW. The locations mentioned in the main text are the Greenland Sea (GS), Fram Strait (FS), Morris Jessup Rise (MJR), Gakkel Ridge (GR), Nansen Basin (NB), Intra Basin (IB), St. Anna Trough (SAT), Makarov Basin (MB), Amundsen Basin (AB), Lomonosov Ridge (LR), and Laptev Sea (LS).

subsequently infer its circulation pathways. In section 2, we describe the data used in this study, the method we use to quantify CBDW, and employ a sensitivity analysis to quantify the uncertainty of our method. In section 3, we present the results from five specific expeditions, yielding a total of nine transects. In section 4, we discuss the circulation pathways of CBDW in the Eurasian Basin, the possible forcing mechanisms for the inflow of CBDW, and the presence and potential

impacts of deep eddies observed in this study. Finally, in section 5, we summarize our study.

## 2. Data and methods

### a. Observational data

Conductivity–temperature–depth (CTD) measurements were collected on board the icebreaker *Oden* from 2 August 2021 to 1 September 2021 as part of SAS. For this study, we use 27 full-depth CTD casts obtained during SAS (Fig. 1a, red lines). Hydrographic measurements were obtained by the standard SeaBird SBE911plus system, with dual sensors for measuring temperature and conductivity and two single sensors for measuring pressure and oxygen. Complete details on all the measurements during SAS and their calibration can be found in the cruise report (Snoeijs-Leijonmalm 2022).

As part of the year-long expedition Multidisciplinary drifting Observatory for the Study of the Arctic Climate (MOSAiC), CTD measurements were collected on board R/V *Polarstern* across much of the Amundsen Basin and Fram Strait from October 2019 to October 2020 (Fig. 1a, yellow lines; Rabe et al. 2022). During this cruise, CTD measurements were collected by a SeaBird SBE911plus system with dual temperature and conductivity and oxygen sensors, as well as a single pressure sensor. More information about the MOSAiC measurements can be found in Rabe et al. (2022) and references therein. The measurements in our study area were all collected during the part of the drift often referred to as legs 1–3 (October 2019–May 2020).

To give as complete an overview of the circulation pathways of CBDW as possible and to analyze any potential temporal variability in the inflow of CBDW, we combine the observations from SAS and MOSAiC with historical observations from the Unified Database for Arctic and Subarctic Hydrography (UDASH; Behrendt et al. 2018). In particular, we focus here on the UDASH observations collected during cruises PS94 (summer 2015), PS80 (summer 2012), and PS78 (summer 2011). We exclude all UDASH data that are not quality flagged as “good,” except for certain profiles that were individually assessed and deemed of good quality. It should be noted that none of the data from these cruises contain data directly from the Intra Basin, where the likely main inflow of CBDW occurs. We calculate Conservative Temperature ( $\Theta$ ) and Absolute Salinity ( $S_A$ ) for all datasets using the International Thermodynamic Equation of Seawater–2010 (TEOS-10; McDougall and Barker 2011). We separate all observations into two groups, the Amerasian Basin group and the Eurasian Basin group, as presented in Fig. 2a.

### b. CBDW content calculation

To detect and quantify the presence of CBDW in the water column, we use an end-member analysis (e.g., Mamayev 1975; Jenkins 1999; Zheng et al. 2021), which has previously been employed for quantifying water masses in the Arctic (e.g., Marnela et al. 2016; Heuzé et al. 2017). The three water masses used in this method are UPDW, CBDW, and EBDW. We use  $\Theta$  and  $S_A$  as tracers. By definition (McDougall and Barker 2011), they are conservative, that is, the properties do

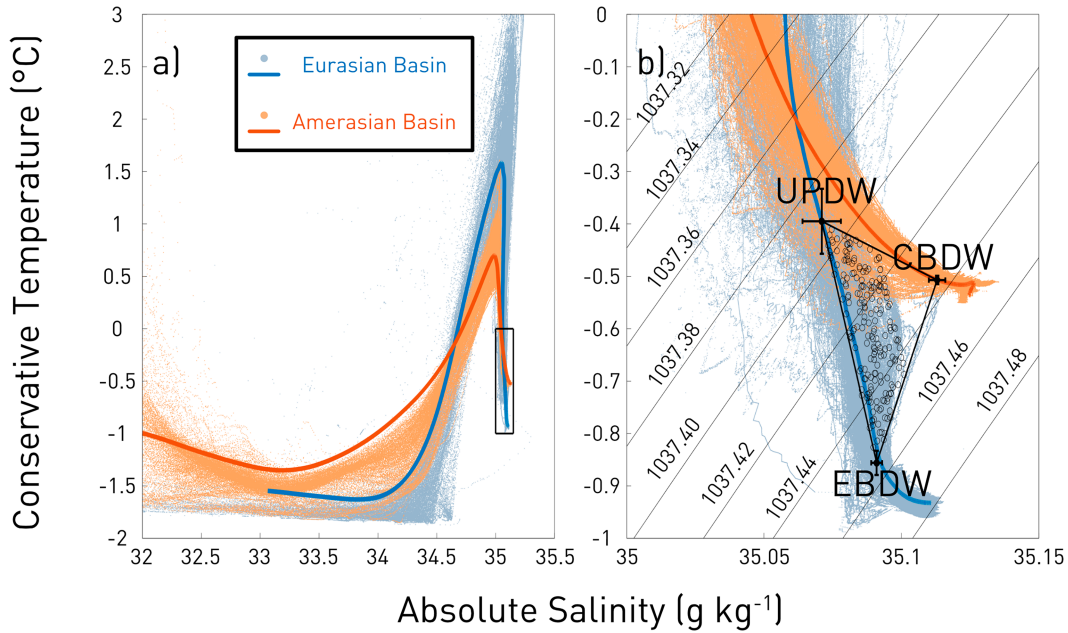


FIG. 2. Hydrographic properties of the Arctic Ocean in a  $\Theta$ - $S_A$  diagram. (a) Small dots show individual measurements and thick lines show depth-averaged values run through a 20-m moving average filter in the Eurasian Basin (blue) and the Amerasian Basin (red). The deep waters are in the black rectangle, zoomed in on the right panel. (b) Zoomed-in version of (a). Thin black diagonal lines show the isopycnals, referenced to 2000 dbar. The black error bars show the mean and the standard deviation in the  $\Theta$ - $S_A$  space for the three water masses discussed in this study: UPDW, CBDW, and EBDW. Thick black lines show the mixing triangle, drawn from the end points of these water masses (see Table 1). Hollow, black circles are the simulated measurements of CBDW, used in the sensitivity analysis (see section 2c).

not change except through physical mixing with another water mass. Three mixing lines connect the characteristic properties, or end points, of UPDW, CBDW, and EBDW in the  $\Theta$ - $S_A$  space, forming a triangular mixing space (see Fig. 2b). The properties of a pure mixture between any two of the water masses evolve linearly along their mixing line. Any sample's relative composition of these three water masses is then determined by calculating the distance to the lines. The fraction of CBDW is given by

$$\phi_{\text{CBDW}} = \frac{\Theta_{\text{Obs}} - \Theta_{\text{EBDW}} - \frac{(S_{A_{\text{Obs}}} - S_{A_{\text{EBDW}}})(\Theta_{\text{UPDW}} - \Theta_{\text{EBDW}})}{S_{A_{\text{UPDW}}} - S_{A_{\text{EBDW}}}}}{\Theta_{\text{CBDW}} - \Theta_{\text{EBDW}} - \frac{(S_{A_{\text{CBDW}}} - S_{A_{\text{EBDW}}})(\Theta_{\text{UPDW}} - \Theta_{\text{EBDW}})}{S_{A_{\text{UPDW}}} - S_{A_{\text{EBDW}}}}}, \quad (1)$$

where  $\phi_{\text{CBDW}}$  is the content of CBDW, and  $\Theta$  and  $S_A$  with the different subscripts denote the observed properties in the

water column or the end points of the three distinct water masses.

The end points were not chosen following previous literature, for example, Rudels et al. (2002). Although commonly used, their water mass definitions were derived for the Fram Strait and are therefore not suitable for the purposes of this study. Instead, we chose the water mass properties as basin-wide averages in the Eurasian and Amerasian Basins at a depth level close to that of the sill of the Intra Basin, which has been found to be at an 1870-m depth (Björk et al. 2007) and where the main inflow of CBDW has been observed (Björk et al. 2010). The end points were calculated as the mean of a density range that is likely to contribute to the observed mixing between the water masses (listed in Table 1). Had we chosen definitions based on, for example, Rudels et al. (2002), UPDW would have incorporated everything between the Atlantic Water layer and the deeper water masses. However, even the largest intrusion of CBDW we observe (Fig. A1, green line) is constrained to a small density range between 1037.4 and

TABLE 1. The water masses discussed in the text, their observed properties as the mean and the standard deviation, and the density ranges we set to classify them.

Water mass	$\Theta$ (°C)	$S_A$ (g kg <sup>-1</sup> )	Water mass boundaries
UPDW	-0.395 ± 0.062	35.071 ± 0.007	37.38 < $\sigma_2$ < 37.40, 35.05 < $S_A$ < 35.10
CBDW	-0.507 ± 0.008	35.113 ± 0.003	37.43 < $\sigma_2$ < 37.44, -0.55 < $\Theta$ < -0.45
EBDW	-0.856 ± 0.023	35.091 ± 0.002	37.45 < $\sigma_2$ < 37.46, 35.085 < $S_A$ < 35.10

$1037.44 \text{ kg m}^{-3}$  and mainly mixes isopycnic with ambient waters. We thus set a relatively constrained density range compared to previous water mass classifications, as the intrusions of CBDW are vertically confined to a small part of the water column. The properties of the three water masses used and their definitions are given in Table 1 and Fig. 2b. In all figures showing transects, we also mask everything above the upper bound of UPDW and below the lower bound of EBDW. Additionally, we have added a mesh with white crosses to all transects in the UPDW range, as warm and salty UPDW outside of the mixing triangle can result in a false CBDW signal.

### c. Robustness of the chosen end points

To quantify the uncertainty of the chosen end points we perform a sensitivity analysis by running a Monte Carlo simulation with 200 randomly distributed hydrographic measurements, based on the method of Zheng et al. (2021). All simulated measurements  $\phi_{\text{sim}}$  lie within the triangular mixing space formed by the UPDW–CBDW–EBDW mixing lines and are limited by a maximum CBDW content of  $500 \text{ g kg}^{-1}$ , as most observed values of the intrusion are within this range (see Fig. 2). The end points are perturbed 5000 times within the observed variability for each water mass (Table 1). We then recalculate the CBDW content for each measurement with the new perturbed end points, resulting in 1000000 CBDW fractions, which we call  $\phi_{\text{per}}$ . We ran several sets of simulations, where either all three end points were perturbed simultaneously or just one end point was perturbed, allowing us to estimate which water mass carries the highest uncertainty.

By plotting histograms of the difference between the simulated CBDW fractions and the CBDW fractions with the perturbed end points ( $\phi_{\text{sim}} - \phi_{\text{per}}$ ), we can observe the distribution of the CBDW content bias arising from the uncertainty of the chosen end points (Fig. 3). We calculate the standard deviation of the difference between  $\phi_{\text{sim}}$  and  $\phi_{\text{per}}$  as a metric of the uncertainty of each water mass.

From the spread of the histograms when we only perturb individual water masses (Figs. 3b–d), we can clearly see that UPDW represents almost all the uncertainty in the chosen end points. With an uncertainty of  $\pm 58.19 \text{ g kg}^{-1}$ , it is approximately 4 times as large as that of CBDW and EBDW, which cause uncertainties of  $\pm 13.98$  and  $\pm 16.29 \text{ g kg}^{-1}$ , respectively. In Fig. 2b, we can see that UPDW occupies a relatively large part of the  $T$ – $S$  space compared to CBDW and EBDW. Yet our definition still greatly reduces the uncertainty of the UPDW compared to previous water mass definitions (e.g., Rudels et al. 2002), where UPDW would incorporate virtually everything between the Atlantic Water layer and the deeper water masses. When we perturb all end points simultaneously, the uncertainty is  $\pm 61.42 \text{ g kg}^{-1}$ , which is about 20%–30% of the CBDW content of the recirculating branch along the Gakkel Ridge. Of course, the relative uncertainty goes up where very small intrusions of CBDW are observed. The uncertainty can then be as large as, or even larger than, the measured content of CBDW in the water column. In those instances, we use dissolved oxygen content as an extra tracer for increased robustness in our analyses, as CBDW is oxygen deficient compared to UPDW

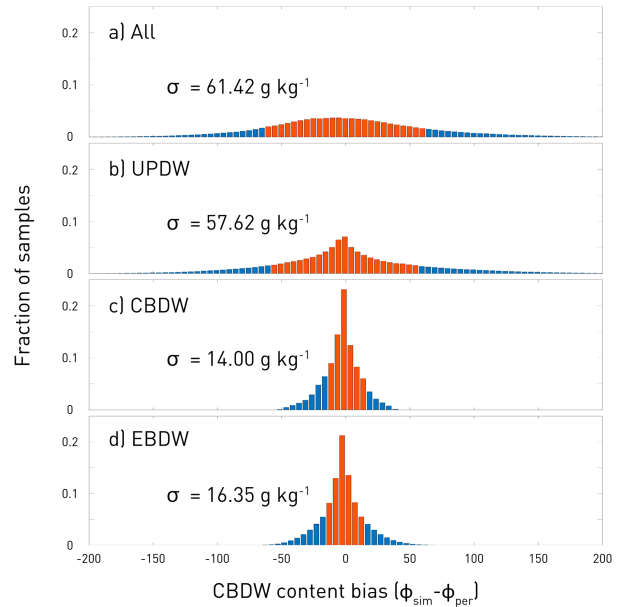


FIG. 3. Histograms showing the spread of the CBDW content bias ( $\phi_{\text{sim}} - \phi_{\text{per}}$ ) arising from the uncertainty in the chosen end points for the Monte Carlo simulations. Four simulations were run where (a) all end points are perturbed, (b) only the UPDW is perturbed, (c) only CBDW is perturbed, and (d) only EBDW is perturbed. All plots show the standard deviation  $\sigma$  as a measure of the uncertainty associated with each water mass. The CBDW content bias within one standard deviation is highlighted in red.

and EBDW (Fig. 4; Björk et al. 2010). As evidenced by hydrographic profiles, there is a distinct oxygen minimum at a 1700–2000-m depth, confirming the inflow (Fig. 4a, purple dots) and recirculation of CBDW within the Eurasian Basin (Fig. 4a, red dots).

Our uncertainty estimations suggest that the CBDW content calculation can be sensitive to the choice of end points. However, those uncertainties are small compared to the CBDW signal we observe and will not make a qualitative change to the pattern of CBDW distribution.

## 3. Results

In this section, we quantify the presence of CBDW from a total of 10 transects in the western Eurasian Basin and in the eastern Eurasian Basin (sections 3a and 3b, respectively).

### a. Western Eurasian Basin

CBDW content estimated from hydrographic profiles in the western Amundsen Basin during cruises SAS, PS94, PS80, and PS78 (red, purple, green, and brown solid lines, respectively, in Fig. 1a) shows a considerable amount of horizontal variability, but a fairly consistent pattern emerges (Figs. 5a–d). There is a persistent CBDW core between the 1600- and 2000-m depth in the Amundsen Basin just by the Gakkel Ridge, with maximum values of  $250$ – $300 \text{ g kg}^{-1}$  (600, 300, 300, and 600 km in Figs. 5a–d, respectively). Above the abyssal plains of the central Amundsen Basin, there is a gradual deepening of the CBDW core along the

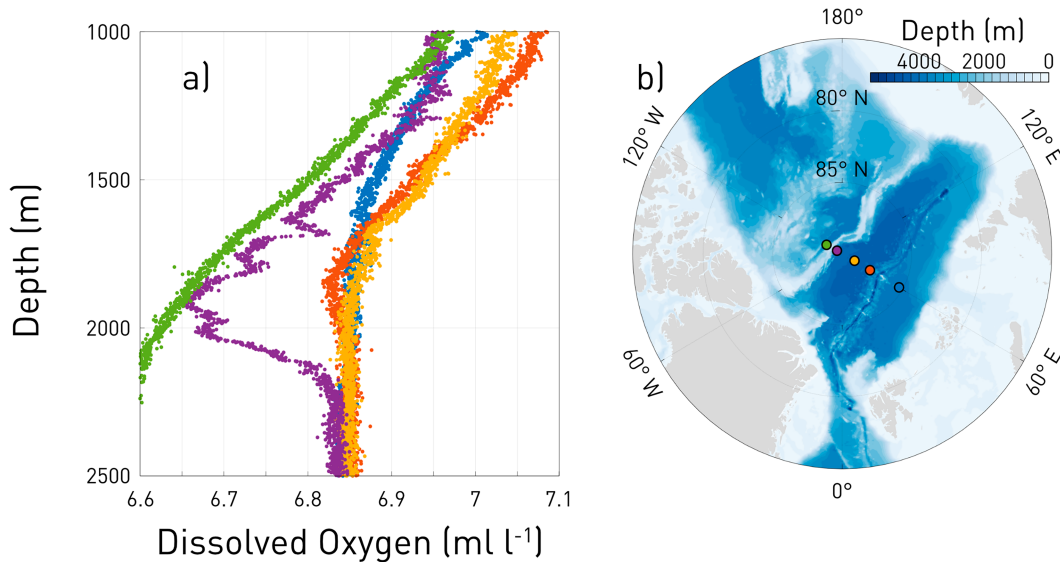


FIG. 4. Representative data of the spatial variability of dissolved oxygen, from *Polarstern* cruise PS94, conducted in 2015. (a) Dots show individual measurements in a vertical profile for the central Nansen Basin (blue), Amundsen Basin side of Gakkel Ridge (red), central Amundsen Basin (yellow), Amundsen Basin side of Lomonosov Ridge (purple), and Makarov Basin (green). Note the strong oxygen minimum at Lomonosov Ridge (purple), and the weaker oxygen minimum at Gakkel Ridge (red), highlighting the inflow and recirculation of CBDW in the Eurasian Basin. (b) Stereographic projection showing the bathymetry of the Arctic Ocean (blue-white color scale). The locations of the hydrographic data shown in (a) are denoted by the colored dots.

isopycnals, as well as a concurrent decrease of CBDW content, with maximum values of  $150\text{--}200\text{ g kg}^{-1}$  (Figs. 5a–d). Additionally, a considerable amount of interleaving is detected (see Fig. A1 in appendix A), suggesting a high degree of double-diffusive mixing, a common feature in the typically quiescent Arctic Ocean (Schulz et al. 2022; Polyakov et al. 2019; Shibley et al. 2017). The persistently higher CBDW content at the Gakkel Ridge compared to the interior Amundsen Basin suggests the presence of a boundary flow along the Gakkel Ridge being transported eastward.

Directly downstream of the Intra Basin, where the main inflow of CBDW is thought to occur (Björk et al. 2010), strong intrusions of CBDW are identified close to the Lomonosov Ridge (600 km in Fig. 5b, 850 km in Fig. 5d). These inflows stretch from a 1400- to a 2200-m depth and have cores of  $980$  and  $825\text{ g kg}^{-1}$  (Figs. 5b and 5d), respectively, that is, they contain almost completely unmodified CBDW. Approximately 450 km farther downstream of the Intra Basin, a distinct CBDW signature is detected in a transect conducted during SAS between the Lomonosov Ridge and the Morris Jessup Rise (Fig. 1a, red dashed line; Fig. 6). CBDW is detected from a 1500- to a 2500-m depth, with a maximum CBDW content of  $600\text{ g kg}^{-1}$  at the 2000-m depth. This finding is consistent with previous observations, which have shown inflows of similar magnitude directly in the Intra Basin and along the Lomonosov Ridge (Björk et al. 2010), suggesting that it may be a common occurrence.

Comparing the transects between the years, some notable dynamics are observed. In particular, what appears to be an eddy is detected in the Amundsen Basin in 2021 (encircled in Fig. 5a). The feature is located above the abyssal plains, far

from any boundaries, and stretches from a 1600- to a 2200-m depth, that is, within the observed depth range of CBDW inflow (see Figs. 5b,d), with a CBDW content of  $600\text{ g kg}^{-1}$  at the 2000-m depth. Additionally, vertically displaced isopycnals are detected, with relatively light waters below the feature compared to the adjacent water at the same depth, indicative of an anticyclonic rotation (e.g., Meneghello et al. 2021). Hence, we suggest that the feature is caused by an anticyclonic eddy that has split off from the boundary current somewhere between the Intra Basin and the Morris Jessup Rise, where similarly high CBDW content has been observed (Figs. 5b,d and 6). We will come back to this hypothesis in section 4c.

Furthermore, while almost unmodified CBDW inflows are observed at the Lomonosov Ridge, just downstream of the Intra Basin, in 2015 and 2011 (Figs. 5b and 5d, respectively), no CBDW content is detected there in 2021 (Fig. 5a). This suggests that the inflow of CBDW into the Amundsen Basin is intermittent in its nature.

Overall, these results confirm previous studies highlighting a flow of CBDW along the Lomonosov Ridge and the Greenland continental shelf (Björk et al. 2010). They further suggest a return flow carrying CBDW eastward along the Gakkel Ridge. The quiescent interior appears to get modified on longer time scales through spreading along isopycnals, as well as by comparatively energetic large eddies carrying CBDW away from the boundaries.

#### b. Eastern Eurasian Basin

At the start of the MOSAiC drift (yellow line, Fig. 1a), what appears to be a large eddy is observed in the eastern Amundsen

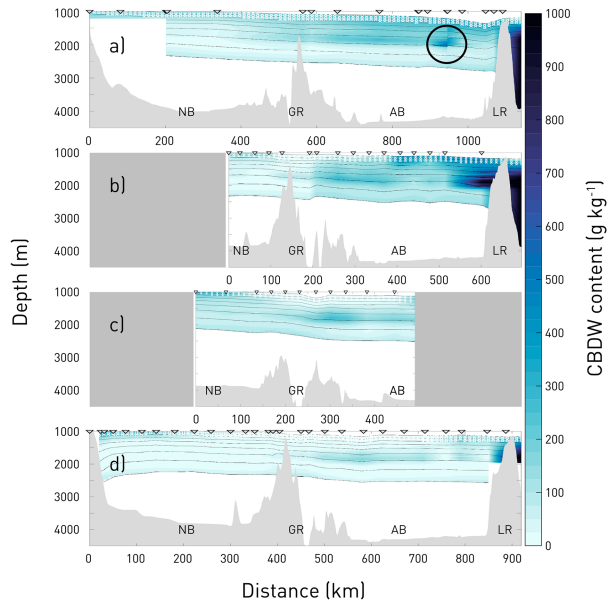


FIG. 5. Estimated CBDW content from CTD data collected across the western Eurasian Basin during (a) SAS in summer 2021 (Fig. 1a, solid red line), (b) PS94 in summer 2015 (Fig. 1a, solid purple line), (c) PS80 in summer 2012 (Fig. 1a, solid green line), and (d) PS78 in summer 2011 (Fig. 1a, solid brown line). Dark colors indicate high CBDW content. The black circle in (a) highlights the location of an eddy. Black contours show the location of an eddy. Black contours show the location of an eddy. Black contours show the location of an eddy. Spacing between the isopycnals is  $0.01 \text{ kg m}^{-3}$ . Data above isopycnal 37.38 and below 37.46 have been masked. Additionally, data within the UPDW range have been masked with white crosses. The gray mask is the bathymetry (IBCAO; Jakobsson et al. 2020), and white triangles at the top of the panels show the location of the CTD profiles. The sections have been aligned by the major bathymetric features. Note the different horizontal scales.

Basin (encircled in Fig. 7). CBDW content is detected between a 1200- and a 2400-m depth, with maximum values of  $500 \text{ g kg}^{-1}$  at the 2000-m depth. Isopycnals above and below the eddy are vertically displaced by up to 200 m, with relatively light waters below the eddy and denser waters above, relative to adjacent water at

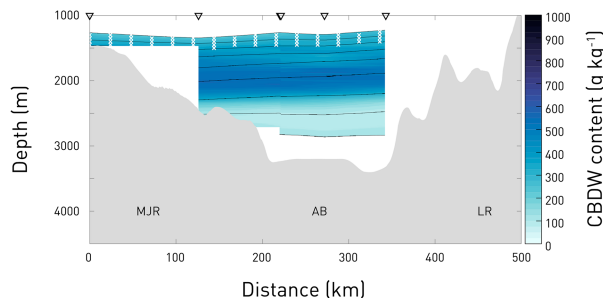


FIG. 6. As in Fig. 5, but collected during SAS in summer 2021 in the westernmost parts of the Amundsen Basin (Fig. 1a, red dashed line).

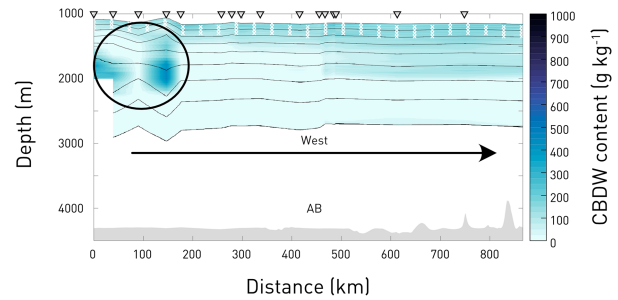


FIG. 7. As in Figs. 5 and 6, but collected during MOSAiC legs 1–3 in 2019/20, drifting in the Amundsen Basin (Fig. 1a, yellow line). The black circle highlights the location of an eddy, which was drifted over twice. The arrow indicates a westerly direction.

the same depth level. Similar to the eddy observed in Fig. 5a, this is indicative of an anticyclonic rotation.

The transect in Fig. 7 further reveals a weak local CBDW maximum centered at a 1900-m depth. A general increase of CBDW content is observed in a westerly direction. In the eastern Amundsen Basin, CBDW content ranges from 50 to  $100 \text{ g kg}^{-1}$  (500 km in Fig. 7), which is close to the estimated uncertainty arising from the choice of end points. However, profiles of dissolved oxygen confirm the presence of CBDW, evidenced by an oxygen minimum at a 1700-m depth (Fig. A2). Farther west, CBDW content reaches up to  $150 \text{ g kg}^{-1}$  (800 km in Fig. 7), consistent with measurements in the western Amundsen Basin (see Figs. 5a–d).

The transect in Fig. 8a reveals the presence of CBDW as far as  $110^\circ\text{E}$  along the Gakkel Ridge (purple dashed line, Fig. 1a). Weak CBDW properties are detected in two casts close to the Gakkel Ridge between a 1600- and a 2000-m depth, with a maximum content of  $80 \text{ g kg}^{-1}$ . The presence of CBDW is confirmed using profiles of dissolved oxygen, showing a small but distinct minimum at an 1800-m depth (Fig. A3). The CBDW signal carried with the return flow along the Gakkel Ridge is, however, absent at  $120^\circ\text{E}$  in 2012 and 2011 (green and brown dashed lines, Fig. 1a; Figs. 8b and 8c, respectively).

However, an eddy is observed in the middle of the Gakkel Ridge (encircled in Fig. 8b). The eddy has two layers, with the upper layer stretching between 1100 and 1500 m and the lower layer between a 1500- and a 2400-m depth, and a maximum CBDW content of  $570 \text{ g kg}^{-1}$  at a 1900-m depth. The isopycnals are vertically displaced with a pattern similar to the eddies observed in Figs. 5a and 7, indicative of an anticyclonic rotation. While the deeper layer is certainly composed of CBDW, the upper layer appears to have a different origin. The oxygen content (Fig. A4) reveals a local oxygen maximum at the upper layer, suggesting a water mass younger than CBDW. Comparing the temperature, salinity, and oxygen content of the upper core to all the hydrographic measurements in the Eurasian Basin, we find that it closely resembles the hydrographic properties along the Eurasian continental slope, between the St. Anna Trough and the Laptev Sea (see Fig. A4). Therefore, it is likely that the eddy has split off from the boundary current at some point and drifted to the Gakkel Ridge.

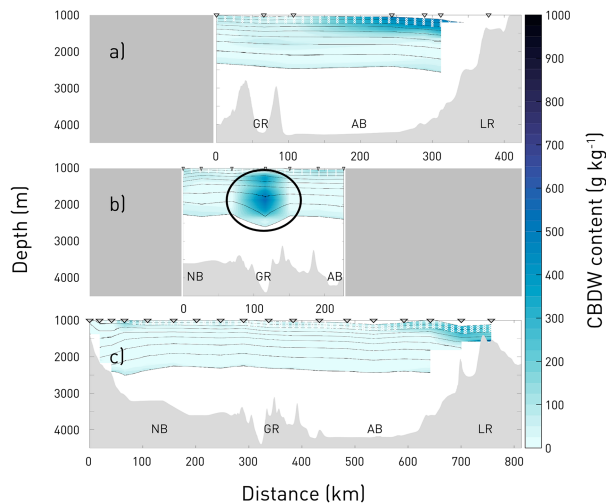


FIG. 8. As in Figs. 5–7, but collected in the eastern Amundsen Basin with the transects starting between 110° and 120° E during (a) PS94 in summer 2015 (Fig. 1a, purple dashed line), (b) PS80 in summer 2012 (Fig. 1a, green dashed line), and (c) PS78 in summer 2011 (Fig. 1a, blue dashed line). The black circle in (b) highlights the location of an eddy. The sections have been aligned by the major bathymetric features. Note the different horizontal scales between the panels.

Overall, these results show that the return flow along the Gakkel Ridge carries CBDW at least as far as 110°E. It should be noted that the estimated CBDW content at 110°E is close to the estimated uncertainty, making it difficult to confirm its presence that far east. However, profiles of dissolved oxygen confirm the presence of CBDW. Additionally, large deep eddies detected in the eastern Amundsen Basin have a vertical extent of up to 1200 m, thus carrying CBDW in up to a quarter of the water column.

#### 4. Discussion

##### a. Circulation pathways

At times, we observe almost unmodified CBDW at the Lomonosov Ridge, just downstream of the Intra Basin (Figs. 5b,d). This corroborates previous findings stating that the main inflow of CBDW occurs at the Intra Basin (Björk et al. 2010), which has been found to have the deepest sill at a depth of approximately 1900 m (Björk et al. 2007). The depth level of the sill corresponds very well with the observed CBDW signal in the Amundsen Basin, which shows maximum values of between a 1700- and a 2000-m depth (e.g., Figs. 5a–d). Nevertheless, in 2021, we found no CBDW at the Lomonosov Ridge (Fig. 5a), suggesting that the inflow of CBDW must be intermittent. However, we did find CBDW content of 550–600 g kg<sup>-1</sup> between a 1500- and a 2500-m depth approximately 450 km downstream along the Lomonosov Ridge, close to Greenland (Fig. 6). This again agrees with previous findings stating that the inflow of CBDW is tightly confined to a boundary flow along the Lomonosov Ridge toward Greenland (Björk et al. 2010). Based on a year-long mooring record in the eastern Amundsen Basin, the

mean velocity at a 1700-m depth was estimated to be 2.4 cm s<sup>-1</sup> (Woodgate et al. 2001). If we assume a similar velocity, then the inflow of CBDW seen in Fig. 6 in September 2021 could have occurred in March 2021 at the Intra Basin. This would mean that the inflow of CBDW is not only intermittent in its nature, but that it could vary on subannual time scales. It should be noted that intermittent inflows might lead to the creation of eddies. The inflow of CBDW along the Lomonosov Ridge and the return flow along the Gakkel Ridge thus likely consist of a series of eddies or remnants of passing eddies, rather than a continuous flow (e.g., Schauer et al. 2002).

CBDW has also been observed in the western parts of the Fram Strait (e.g., Rudels 1986; Marnela et al. 2016) and was observed as a temperature maximum in the Greenland Sea Gyre (Rudels 1995; Budéus et al. 1998) until 2007, when the overlying waters became warmer than the temperature maximum (Somavilla et al. 2013). Therefore, the CBDW inflow continues along the continental slope of Greenland, before exiting through the Fram Strait. However, it is evident that a part of the boundary flow splits off north of the Fram Strait and then recirculates in the Amundsen Basin, as we find a persistent core of CBDW of 200–300 g kg<sup>-1</sup> between a 1700- and a 1900-m depth over the slope of the Gakkel Ridge (Figs. 5a–d). We also find a weak CBDW signal in the Nansen Basin (Figs. 5b–d), suggesting some degree of property transfer across the Gakkel Ridge. Interestingly, we find that the CBDW that recirculates along the Gakkel Ridge has the same density as the CBDW seen at a 2500-m depth north of Greenland. This suggests that the deeper parts of the inflow could be blocked and cannot exit through the Fram Strait and then may spread upward along the isopycnals into the Amundsen Basin.

Furthermore, we find that the recirculating branch then continues along the Gakkel Ridge at least until 110°E (Fig. 8a), much farther east than previously reported, although individual eddies have been identified in the area (Schauer et al. 2002). However, the CBDW content in the eastern Amundsen Basin is close to the estimated uncertainty of 61.42 g kg<sup>-1</sup>, with a maximum content of only 80 g kg<sup>-1</sup> (Fig. 8a). This might be the result of temporal variability upstream that we are not capturing due to too sparse sampling. The weaker or even absent CBDW signal in the eastern Amundsen Basin (Figs. 8a–c), compared to the western Amundsen Basin (Figs. 5a–d), is consistent with hydrographic measurements from the MOSAiC drift (Fig. 7), which exhibit a similar east–west gradient. This indicates that the CBDW signal has become diluted through mixing with ambient waters. Furthermore, the transects in Figs. 8b and 8c are located 160 km farther east along the Gakkel Ridge compared to Fig. 8a. Thus, it is possible that the CBDW signal along the Gakkel Ridge has entirely dissipated by then.

In the interior Amundsen Basin, we find consistently weaker CBDW properties compared to the boundaries (Figs. 5a–d). We also observe substantially more interleaving in the interior (see Fig. A1), a clear sign of a very quiescent environment where diffusive processes are dominant (Polyakov et al. 2019; Shibley et al. 2017). Analyzing the density field, we observe a deepening of the isopycnals into the Amundsen Basin (Figs. 5a–d). Again, this suggests that the interior obtains its properties through

spreading along isopycnals, as has been shown in previous studies (Rudels et al. 2013).

Aside from the Intra Basin, a number of other pathways have been suggested for the inflow of CBDW. Based on a map by Perry et al. (1986), which indicated the deepest passage (2000 m) across the Lomonosov Ridge was north of Greenland, Jones et al. (1995) proposed that the main inflow occurred north of Greenland, where the Lomonosov Ridge meets the Greenland shelf. However, the latest version of the International Bathymetric Chart of the Arctic Ocean (IBCAO) suggests that the passage is only 1200 m deep (Jakobsson et al. 2020), making it an unlikely passage for CBDW, as the CBDW would have to sink over 500 m straight after entering the Amundsen Basin to reach the observed depth levels of the intrusion. At present, there is no observation suggesting that there is a horizontal density gradient at that depth level capable of producing such a deepening. We find no evidence for it in our observations either. The transect from the Lomonosov Ridge to the Morris Jessup Rise (Fig. 6) would likely cover such a flow, as it would move along the slope of the Morris Jessup Rise. The profiles close to the Morris Jessup Rise carry a very similar CBDW content to the profiles at the Lomonosov Ridge (Fig. 6), indicating that the intrusion most likely comes from even farther upstream, most likely the Intra Basin.

Additionally, two passages on the eastern side of the Lomonosov Ridge were mapped in 2014, one at 84°N and one where the Lomonosov Ridge meets the Laptev Sea at 80°N (Björk et al. 2018). The northern passage has a relatively shallow sill with a depth of 1470 m and is therefore not likely to make a significant contribution to the inflow of CBDW. The southern passage, however, has a sill with a depth of 1700 m. Björk et al. (2018) also showed the presence of almost unmodified CBDW at the bottom of the trough. In fact, the temperature and salinity at the passages were the same as those found 200–400 m deeper in the Makarov Basin. This suggests that rather deep waters can be uplifted and advected across the sill, most likely by the boundary current, as suspected by Rudels et al. (2000).

### b. Possible forcing mechanisms

The forcing mechanisms for the exchange of deep waters across the sill in the Intra Basin are still unknown. While we cannot point toward any single forcing mechanism in this study, we appear able to rule some out. Most studies have considered the flow of EBDW to the Amerasian Basin (e.g., Timmermans et al. 2005; Timmermans and Garrett 2006; Rudels 2012), but not drivers for flows of CBDW into the Eurasian Basin. In the absence of better hypotheses, we consider these mechanisms as well. One such possible mechanism is density-driven overflows. However, we find no large displacements of isopycnals across the Lomonosov Ridge that would indicate an overflow (see Figs. 5a,b,d). Previous studies have also shown that the density difference between EBDW and CBDW at a 2000-m depth is only 0.002 kg m<sup>-3</sup> (Björk et al. 2010). This is two orders of magnitude smaller than the dense water cascading observed on the Arctic shelves of 0.39 kg m<sup>-3</sup> (Ivanov et al. 2004) or the Denmark Strait overflow of 0.34 kg m<sup>-3</sup> (Köhl et al. 2007). For

additional comparison, the density difference between EBDW and GSDW at a 2500-m depth across the Fram Strait was estimated to be 0.007 kg m<sup>-3</sup> and was ruled out as a leading-order forcing mechanism for cross-sill advection (von Appen et al. 2015). Additionally, EBDW is denser than CBDW, so overflows are more likely to occur in the other direction (Timmermans et al. 2005; Timmermans and Garrett 2006). The horizontal density gradient across the Lomonosov Ridge is therefore likely to be too small to produce an overflow of CBDW into the Eurasian Basin. An important caveat to note is that overflows are often highly intermittent and can even vary on tidal time scales (e.g., Vlasenko and Stashchuk 2018). We cannot therefore completely eliminate it as a forcing mechanism with our current dataset, which is a few quasi-synoptic transects spaced years apart.

Rudels (2012) instead suggested the pressure gradient across the sill as a mechanism for driving the intermittent exchange of deep waters. Following Rudels (2012), we computed the dynamic height as

$$D = -\frac{1}{g} \int_{p_0}^p \frac{1}{\rho} dp, \quad (2)$$

where  $g$  is the gravitational acceleration,  $p_0$  is the surface pressure,  $p$  is the pressure, and  $\rho$  is the in situ density computed from  $\Theta$  and  $S_A$ , and compare its extrema at 2000 dbar on either side of the Lomonosov Ridge (Table 2). In 2005, when Björk et al. (2010) found CBDW in the Amundsen Basin, the dynamic height was larger in the Amundsen Basin than in the Makarov Basin (up to +0.73 m). This would result in a negative pressure gradient from the Makarov Basin, which would favor a flow of CBDW into the Amundsen Basin. However, in all transects across the Lomonosov Ridge used in this study, the dynamic height was larger in the Makarov Basin, that is, the difference in absolute values was negative (Table 2, rows  $|A| - |M|$ ). According to, for example, Rudels (2012), this would thus not favor a flow of CBDW into the Amundsen Basin. While we could not detect an inflow of CBDW at the Lomonosov Ridge in 2021 (Fig. 5a), there were clear inflows in 2015 and 2011 (Figs. 5b,d), despite their negative dynamic height difference. This suggests that the pressure gradient across the Lomonosov Ridge is not the primary driver for the flow of CBDW into the Eurasian Basin.

Finally, in the Fram Strait, it was found that cross-sill advection at the bottom was driven by upper-ocean mesoscale flows with a period of 1–3 weeks (von Appen et al. 2015). It is possible that similar forcing mechanisms drive the intermittent deep flows over the Intra Basin. Mooring measurements would, however, be required to confirm this forcing mechanism.

### c. Deep eddies

In total, we observe three deep eddies composed of high CBDW content in our results, with a CBDW content of up to 600 g kg<sup>-1</sup> (Figs. 5a, 7, and 8b). These eddies are rather striking features, at times stretching over 1200 m in vertical extent (Fig. 7), thus carrying CBDW properties in up to a quarter of the water column. However, it is hard to say whether we are resolving the full extent of the eddies, as the sparse nature of CTD transects does not allow us to estimate whether we are



TABLE 2. Range in dynamic height (m) referred to the surface at 2000 dbar in the vicinity of the Lomonosov Ridge on the Amundsen ( $A$ ) and Makarov ( $M$ ) sides, and difference between the absolute value of the two ( $|A| - |M|$ ). “Vicinity” is defined as the region between the last cast with seafloor depth larger than 4000 m and the last larger than 2000 m [sill depth, for consistency with Rudels (2012)]. For PS78, this definition returned fewer than three deep casts; we extended toward the deep basin to have three casts on each side. *Oden* 2005 also features the Intra Basin (I), defined as a seafloor depth greater than 2000 m within the Lomonosov Ridge region. PS80 in 2012 and MOSAiC in 2019/20 are not included as they did not cross the Lomonosov Ridge. For the location of *Polarstern* (1996) and *Oden* (2005), see Björk et al. (2010). Transects are further separated between “Greenland” (SAS, red dashed line in Fig. 1), “West” (all cruises, solid lines in Fig. 1), and “East” (dashed lines in Fig. 1). As in, e.g., Rudels (2012), a positive value in the  $|A| - |M|$  row favors a flow from the Makarov to the Amundsen Basin.

Expedition (year)	Greenland	West	East
<i>Polarstern</i> (1996)	—	—	$A$ : -2.33 to -2.25 $M$ : -2.43 to -2.35 $ A  -  M $ : -0.18 to -0.02
<i>Oden</i> (2005)	—	$A$ : -3.60 to -3.28 $I$ : -3.25 to -2.97 $M$ : -3.02 to -2.87 $ A  -  M $ : +0.26 to +0.73	—
PS78 (2011)	—	$A$ : -3.14 to -2.98 $M$ : -3.59 to -3.45 $ A  -  M $ : -0.61 to -0.31	$A$ : -3.24 to -3.19 $M$ : -3.81 to -3.53 $ A  -  M $ : -0.62 to -0.29
PS94 (2015)	—	$A$ : -4.04 to -3.32 $M$ : -4.69 to -4.59 $ A  -  M $ : -1.37 to -0.55	$A$ : -3.18 to -3.15 $M$ : -4.32 to -4.08 $ A  -  M $ : -1.17 to -0.90
SAS (2021)	$A$ : -4.47 to -4.45 $M$ : -4.73 to -3.93 $ A  -  M $ : -0.28 to +0.54	$A$ : -3.77 to -1.13 $M$ : -4.49 to -3.37 $ A  -  M $ : -3.36 to -0.40	—

sampling the core of the eddy, or its edges. This means that we could be underestimating the vertical extent of these eddies. The poor horizontal resolution further means that we cannot estimate the horizontal extent of the eddies. However, previous studies have found typical eddy radii of 11–25 km in the deep Canada Basin of the Arctic Ocean (Carpenter and Timmermans 2012) and typical radii of 6–10 km in the deep Amundsen Basin (Pnyushkov et al. 2018). This corresponds roughly to the first baroclinic Rossby radius in the Arctic Ocean (Nurser and Bacon 2014; Timmermans and Marshall 2020). Detecting coherent eddies from the velocity field in the 2000-m layer of the model reveals typical radii of 5–15 km for the regions of the observed deep eddies (see appendix B for details). In addition to the three eddies composed of CBDW, we find another eddy in the eastern section of the Gakkel Ridge (Fig. 8b), which instead originates from the Barents and Kara Sea shelves (Fig. A4). Over time, the inflow over the Barents and Kara Seas has changed to add warmer, more saline, and overall denser water (Dmitrenko et al. 2014, 2015), which is now found at greater depths (Rudels 2021), which can correspond to the same depths as the inflow of CBDW. This highlights the importance of using multiple tracers, such as oxygen (see Fig. 4), to correctly identify water masses.

Associated with the observed eddies are large vertical displacements of the isopycnals throughout most of the water column. The isopycnals are up to 200 m shallower (deeper) above (below) the eddy, with denser waters above the eddy and lighter waters below, relative to adjacent water at the same depth level (black lines in Figs. 5a, 7, and 8b). These features are indicative of anticyclonic eddies, as the water converges toward the center of the eddy and subsequently

downwells. The anticyclonic eddies are consistent with previous observations of deep eddies in the Canadian Arctic, which have been almost exclusively anticyclonic (e.g., Zhao and Timmermans 2015). Carpenter and Timmermans (2012) found that the water column gains negative relative vorticity as it flows over a ridge and becomes compressed. After eddies pass the ridge, it will increase in vertical extent as the surrounding water adjusts to the anomaly in potential vorticity. This agrees well with an inflow of CBDW over the Lomonosov Ridge and the large vertical extent of the observed eddies.

One site for eddy formation could be the trough where the Lomonosov Ridge meets the Siberian shelf (see Fig. 1b). Mooring records in 1996 from both sides of the trough indicated that CBDW crosses the trough and then either deflects north and flows north along the Lomonosov Ridge as a boundary flow (Woodgate et al. 2001) or forms deep eddies and moves into the interior basin (Woodgate et al. 2001; Schauer et al. 2002). Based on the same mooring data, Woodgate et al. (2001) estimated that the inflow of CBDW can be the result of one to five eddies per year. Multiplying the number of eddies with the volume of a deep CBDW eddy observed in 1996, ranging from  $2 \times 10^{11}$  to  $9 \times 10^{11}$  m<sup>3</sup>, results in a volume transport of 0.0063–0.14 Sv (1 Sv  $\equiv 10^6$  m<sup>3</sup> s<sup>-1</sup>) in addition to the 0.02 Sv estimated from the boundary flow transport (Woodgate et al. 2001). The estimated upper-bound inflow of CBDW would then be on the same order of magnitude as the southward transport of EBDW through the Fram Strait, which has been estimated to be  $0.44 \pm 0.09$  Sv (Somavilla et al. 2013). While this is a rough estimate, it could signify that the inflow of CBDW needs to be better considered, especially since the main inflow of CBDW is thought to occur at the Intra Basin (Björk et al. 2007, 2010).

Another site for eddy formation could be the Intra Basin or downstream of it, along the Lomonosov Ridge and the Greenland continental slope. Eddy formation is known to occur in confluence areas of boundary currents (Schauer et al. 2002; Pnyushkov et al. 2018) and by boundary current instabilities (Zhao et al. 2014). Björk et al. (2010) also suggested that the Morris Jessup Rise could be a hotspot for eddy formation. The sharp and steep bathymetry there was found to force some separation of flow along the Morris Jessup Rise, which would then likely result in eddy formation. The results from the model simulation (Fig. B1) show that the boundary currents are the most active formation sites for deep eddies and confirm the regions mentioned above as possible source regions for the observed eddies. A large number of eddies (up to 7 per year and  $100 \text{ km}^2$ ) were first detected where the Lomonosov Ridge meets the Laptev Sea, as well as on the Amundsen Basin side of the Lomonosov Ridge around the Intra Basin (Fig. B1).

The high CBDW content of the eddies suggests that these eddies can trap water efficiently. This is known to happen when the rotational velocity is much larger than the ambient velocity (Chelton et al. 2007). Observations of deep eddies in the Arctic have shown the maximum rotational velocity to be an order of magnitude larger than the advective velocity (Aagaard et al. 2008; Zhao and Timmermans 2015). It is therefore possible that they provide a large contribution to the lateral salt and heat flux toward the deep interior basin, as CBDW is both warmer and saltier than EBDW. For example, the eddy observed in the MOSAiC drift (encircled in Fig. 7) is  $0.16^\circ\text{C}$  warmer than the ambient water at 2000 m, thus providing a potentially important source of heat in the deep Amundsen Basin.

## 5. Conclusions

In this study, we provide an overview of the to-date most complete circulation pathways of CBDW within the Eurasian Arctic from currently available data, by merging hydrographic data from two recent expeditions (MOSAiC and SAS) with historical measurements. We find the presence of CBDW across large parts of the Amundsen Basin, from north of Greenland to the eastern Amundsen Basin (see Fig. 1b). Our findings corroborate previous studies highlighting that the main inflow of CBDW occurs at the Intra Basin at a depth of approximately 1900 m. We also find that the CBDW inflow at the Intra Basin is intermittent, and that it can change on time scales of 6 months or less. The CBDW subsequently flows south, likely as a series of eddies along the Lomonosov Ridge and the Greenland continental slope. However, we find that the deeper parts of the boundary flow turn around somewhere north of the Fram Strait and instead recirculate in the Amundsen Basin along the Gakkel Ridge. The recirculating branch of CBDW is found as far as  $110^\circ\text{E}$ , albeit with a much lower CBDW content of around  $80 \text{ g kg}^{-1}$  (Fig. 8a) compared to at  $60^\circ\text{E}$ , where values of  $300 \text{ g kg}^{-1}$  are found (Figs. 5a–d), suggesting considerable mixing along the way. While CBDW is both warmer and saltier than EBDW, it is unclear to what

extent the recirculating branch influences the water mass properties in the Amundsen Basin.

The forcing mechanisms for deep flows across the Lomonosov Ridge remain unclear as we are limited to a few quasi-synoptic CTD transects across several years, but we appear able to rule out some previously suggested mechanisms. We show that the density difference is likely too small to produce any overflow, although we cannot completely rule out the possibility of intermittent overflows due to the sparsity and low temporal resolution of the data. Furthermore, we also find that the dynamic height was larger in the Makarov Basin for all transects, which would then not favor a flow of CBDW into the Amundsen Basin. This suggests that the pressure gradient across the Lomonosov Ridge is also not a leading driver for cross-sill advection. Continuous observations, such as from full-depth moorings, would be needed to fully determine the dynamics of the inflow, ideally coupled with tracer measurements to investigate its timing.

We observe three deep eddies of CBDW origin in our data, with a maximum CBDW content of  $600 \text{ g kg}^{-1}$  and spanning up to 1200 m in vertical extent. We also observe that the isopycnals are displaced by up to 200 m above and below the eddy. This is indicative of an anticyclonic rotation, similar to observations of deep eddies in the Canada Basin (e.g., Carpenter and Timmermans 2012). The high CBDW content found in the eddies means that they have likely formed where the Lomonosov Ridge meets the Siberian shelf or the Intra Basin, or downstream of it toward Greenland, where similarly high CBDW content has been observed. It is possible that these eddies contribute significantly to the lateral salt and heat flux toward the deep interior, a hypothesis that cannot be verified without routine monitoring of the deep ocean.

*Acknowledgments.* This work is funded by the Swedish Research Council, Grant 2018-03859, awarded to CH. Participation of SK in MOSAiC and SAS was supported by the Swedish Research Polar Secretariat. VM was funded by the EPICA project in the research theme “MARE:N - Polarforschung/MOSAiC” funded by the German Federal Ministry for Education and Research with funding 03F0889A. YZ acknowledges support from the China Scholarship Council, the University of East Anglia, the European Research Council (under H2020-EU.1.1.) Research Grant 741120: Climate-relevant Ocean Measurements and Processes on the Antarctic continental Shelf and Slope (COMPASS), and the NERC Research Grant NE/W007045/1 NSFGEO-NEC: Collaborative Research: Accelerating Thwaites Ecosystem Impacts for the Southern Ocean (ARTEMIS). This work was carried out and data used in this manuscript were produced as part of MOSAiC with the tag MOSAiC20192020 (AWI\_PS122\_00). We thank all those who contributed to MOSAiC and made this endeavor possible (Nixdorf et al. 2021). We similarly thank all those who contributed to SAS, and in particular, the Swedish Polar Research Secretariat. Finally, we thank the two anonymous reviewers and the editor Yueng-Djern Lenn for their comments, which greatly improved this manuscript.

**Data availability statement.** The Multidisciplinary drifting Observatory for the Study of the Arctic Climate (MOSAiC) data were submitted to PANGAEA in September 2022 (<https://doi.pangaea.de/10.1594/PANGAEA.959964> and <https://doi.pangaea.de/10.1594/PANGAEA.959963>). The Synoptic Arctic Survey (SAS) data are freely available via <https://doi.pangaea.de/10.1594/PANGAEA.951266>. Historical data from the Unified Database for Arctic and Subarctic Hydrography (UDASH) are freely available via <https://doi.pangaea.de/10.1594/PANGAEA.872931>. The gridded bathymetry from the International Bathymetric Chart of the Arctic Ocean (IBCAO) is freely available through [https://www.gebco.net/data\\_and\\_products/gridded\\_bathymetry\\_data/arctic\\_ocean/](https://www.gebco.net/data_and_products/gridded_bathymetry_data/arctic_ocean/). The land mask from A Global Self-consistent Hierarchical High-resolution Geography Database (GSSHG) is freely available via <https://www.soest.hawaii.edu/pwessel/gshhg/>. The contact for the model

simulation data is Vasco Müller ([vasco.mueller@awi.de](mailto:vasco.mueller@awi.de)), and the data are available on demand.

## APPENDIX A

### Observational Data

Saline intrusions highlight the inflow of CBDW at Lomonosov Ridge and the recirculation along Gakkel Ridge (Fig. A1). Additionally, profiles of dissolved oxygen show the presence of a large eddy in the Amundsen Basin (Fig. A2) and indicate the presence of CBDW in the eastern Amundsen Basin (Fig. A3). Additional profiles of dissolved oxygen show two eddies in the eastern Amundsen Basin, one composed of CBDW and the other from the continental slope at the Laptev Sea (Fig. A4).

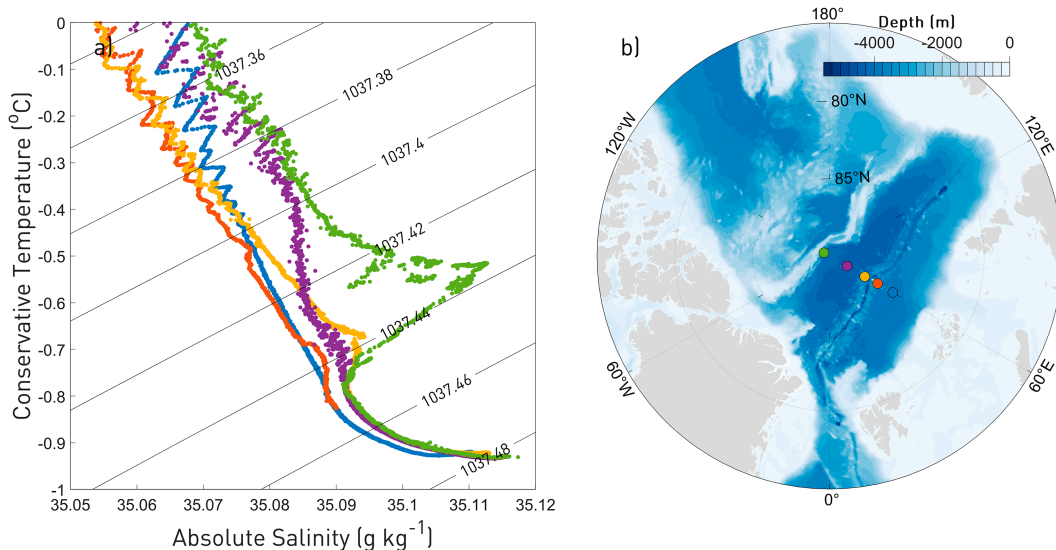


FIG. A1. Representative data of the spatial variability of CBDW from *Polarstern* cruise PS94, conducted in 2015. (a) Small dots show individual measurements in a  $\Theta$ - $S_A$  diagram for the central Nansen Basin (blue), Nansen Basin side of Gakkel Ridge (red), Amundsen Basin side of Gakkel Ridge (yellow), central Amundsen Basin (purple), and Amundsen Basin side of Lomonosov Ridge (green). Black diagonal lines show the isopycnals, referenced to 2000 dbar. Note the weak CBDW properties on the Nansen Basin side of Gakkel Ridge (red dots), as well as the high degree of interleaving in the central Amundsen Basin (purple dots). (b) Stereographic projection showing the bathymetry of the Arctic Ocean (blue–white color scale). The locations of the hydrographic data shown in (a) are denoted by the colored dots.

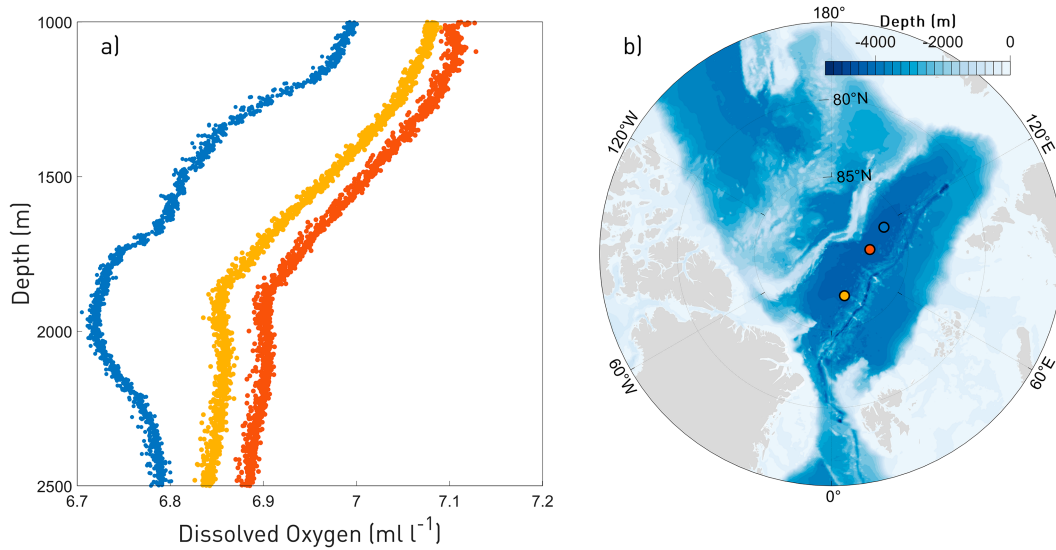


FIG. A2. Exemplary profiles of dissolved oxygen during the MOSAic drift in 2019/20. (a) Dots show individual measurements in a vertical profile for an eddy in the eastern Amundsen Basin containing high amounts of CBDW (blue; encircled in Fig. 7), for the central Amundsen Basin (red), and for the western Amundsen Basin (yellow). Note the oxygen minimum in all profiles at approximately an 1800-m depth, confirming the presence of CBDW. (b) Stereographic projection showing the bathymetry of the Arctic Ocean (blue–white color scale). The locations of the hydrographic data shown in (a) are denoted by the colored dots.

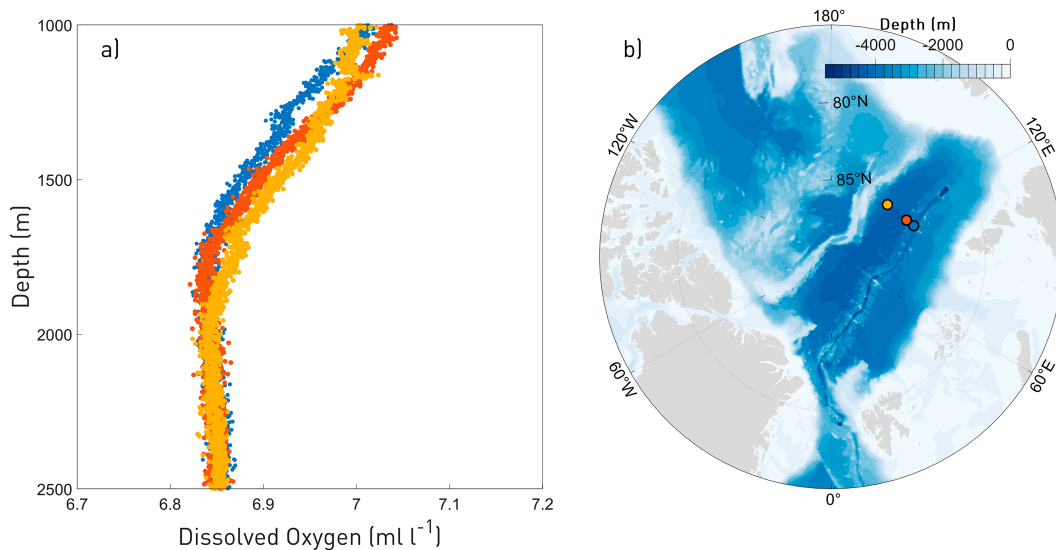


FIG. A3. Exemplary profiles of dissolved oxygen in the eastern Amundsen Basin during *Polarstern* cruise PS94 in 2015. (a) Dots show individual measurements in vertical profiles for Gakkel Ridge (blue and red) and for the interior Amundsen Basin (yellow). Note the oxygen minimum in the profiles close to Gakkel Ridge (blue and red) at approximately an 1800-m depth, confirming the presence of CBDW. (b) Stereographic projection showing the bathymetry of the Arctic Ocean (blue–white color scale). The locations of the hydrographic data shown in (a) are denoted by the colored dots.

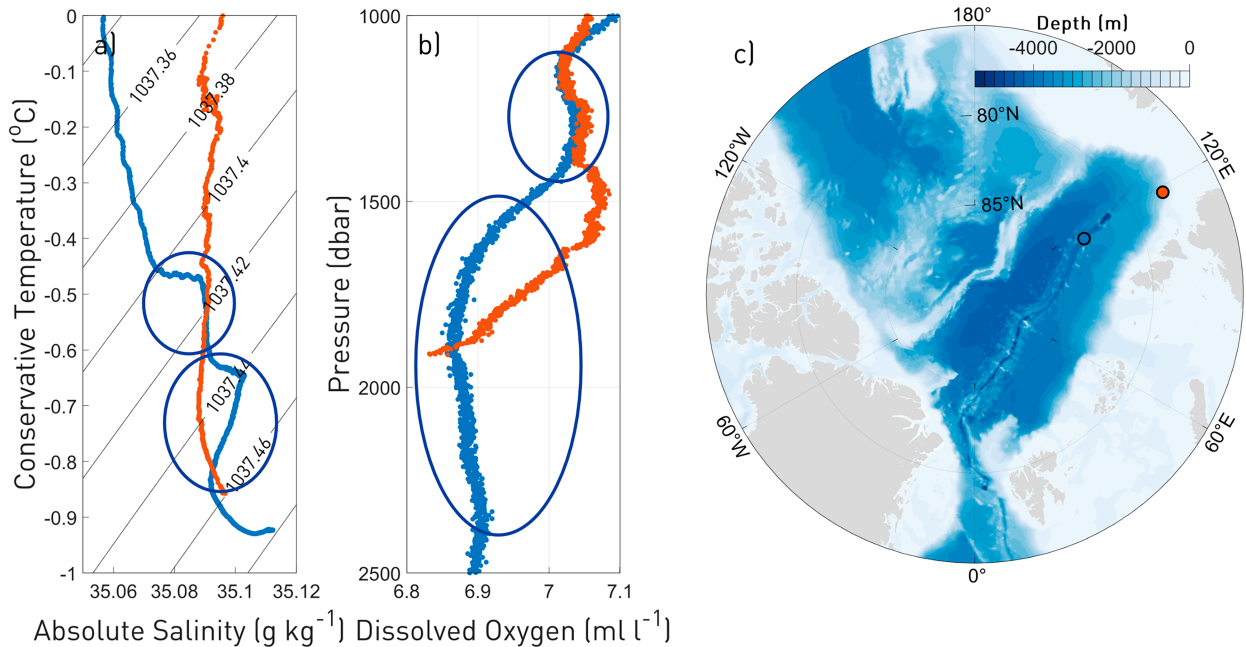


FIG. A4. Comparison of the hydrographic properties from *Polarstern* cruise PS80, conducted in 2012. Blue dots show a profile from Gakkel Ridge (encircled in Fig. 8b), and red dots show a profile from the continental slope of the Laptev Sea, in (a) a  $\Theta$ - $S_A$  diagram and (b) a vertical profile of dissolved oxygen. (c) Stereographic projection showing the bathymetry of the Arctic Ocean (blue-white color scale). The locations of the hydrographic data shown in (a) and (b) are denoted by the colored dots. The dark blue circles in (a) and (b) show the locations of two eddies observed at Gakkel Ridge (blue dots). Note that while the lower eddy shows clear CBDW properties with its oxygen minimum, the upper eddy instead closely resembles properties at the continental slope of the Laptev Sea.

## APPENDIX B

### Model Simulation

The model simulation was carried out with the unstructured grid Finite-Volume Sea Ice–Ocean Model, version 2 (Fig. B1; FESOM2; Danilov et al. 2017), allowing the use of variable resolution without the need for nesting. The high-resolution setup of the model was first introduced by Wang et al. (2020), with a horizontal resolution of 1 km in the Arctic, allowing for a realistic representation of the eddy field, and 30 km in the global ocean. In the vertical, 70  $z$  levels are

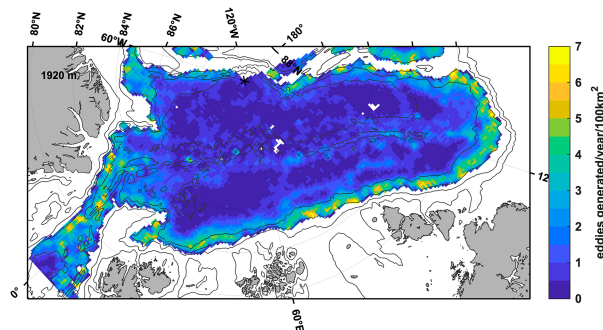


FIG. B1. Number of eddies generated in the model simulation per year and  $100 \text{ km}^2$  (blue–yellow color scale). Isobaths are indicated every 1000 m by the black lines.

used. The model was initialized from PHC3 climatology (Steele et al. 2001), starting from the year 2010 and was run for 10 years using atmospheric forcing from the Japanese 55-year Reanalysis (JRA-55) v.1.4 (Tsujino et al. 2018).

Eddies in the model were detected using the vector-geometry-based algorithm by Nencioli et al. (2010). The algorithm has been used successfully to detect eddies from the velocity field of both observational and model data (e.g., Liu et al. 2012; Müller et al. 2017, 2019; Wekerle et al. 2020). Since the algorithm requires data on a regular mesh, the model output was first rotated toward the equator (to avoid the singularity of the North Pole) and then interpolated from the original unstructured grid to a regular mesh. While this specific algorithm is computationally more expensive than those algorithms based on closed contours of sea level anomalies (e.g., Chelton et al. 2011; Mason et al. 2014), it allows for the detection of eddies on any depth level, which is crucial for the present study of the deep Amundsen Basin. Eddy centers are detected based on four constraints:

- 1) The  $u$  component has to reverse in sign along an east–west section across the eddy center, and the magnitude of  $u$  has to increase away from it.
- 2) The  $v$  component has to reverse in sign along a north–south section across the eddy center, and the magnitude of  $v$  has to increase away from it; (the sense of rotation has to match  $v$ ).

- 3) The potential eddy center has to be a local minimum of velocity magnitude.
- 4) The sign of vorticity cannot change around the eddy center.

The outer boundary of a detected eddy is then defined as the largest closed contour of the local streamfunction around the eddy center, and the eddy radius is defined as the radius of a circle with the same area as the one enclosed by the outer boundary. After the eddies are detected, eddy tracks are computed by comparing eddy centers in consecutive time steps and matching eddies with the same sense of rotation to determine the eddy trajectories all the way to their source region.

#### REFERENCES

- Aagaard, K., R. Andersen, J. Swift, and J. Johnson, 2008: A large eddy in the central Arctic Ocean. *Geophys. Res. Lett.*, **35**, L09601, <https://doi.org/10.1029/2008GL033461>.
- Anderson, L. G., and Coauthors, 1994: Water masses and circulation in the Eurasian Basin: Results from the *Oden* 91 expedition. *J. Geophys. Res.*, **99**, 3273–3283, <https://doi.org/10.1029/93JC02977>.
- Behrendt, A., H. Sumata, B. Rabe, and U. Schauer, 2018: UDASH—Unified Database for Arctic and Subarctic Hydrography. *Earth Syst. Sci. Data*, **10**, 1119–1138, <https://doi.org/10.5194/essd-10-1119-2018>.
- Björk, G., and Coauthors, 2007: Bathymetry and deep-water exchange across the central Lomonosov Ridge at 88–89°N. *Deep-Sea Res. I*, **54**, 1197–1208, <https://doi.org/10.1016/j.dsr.2007.05.010>.
- , and Coauthors, 2010: Flow of Canadian Basin Deep Water in the western Eurasian Basin of the Arctic Ocean. *Deep-Sea Res. I*, **57**, 577–586, <https://doi.org/10.1016/j.dsr.2010.01.006>.
- , M. Jakobsson, K. Assmann, L. G. Andersson, J. Nilsson, C. Stranne, and L. Mayer, 2018: Bathymetry and oceanic flow structure at two deep passages crossing the Lomonosov Ridge. *Ocean Sci.*, **14**, 1–13, <https://doi.org/10.5194/os-14-1-2018>.
- Budéus, G., W. Schneider, and G. Krause, 1998: Winter convective events and bottom water warming in the Greenland Sea. *J. Geophys. Res.*, **103**, 18 513–18 527, <https://doi.org/10.1029/98JC01563>.
- Carpenter, J. R., and M. L. Timmermans, 2012: Deep mesoscale eddies in the Canada Basin, Arctic Ocean. *Geophys. Res. Lett.*, **39**, L20602, <https://doi.org/10.1029/2012GL053025>.
- Chelton, D. B., M. G. Schlax, R. M. Samelson, and R. A. de Szoeke, 2007: Global observations of large oceanic eddies. *Geophys. Res. Lett.*, **34**, 15606, <https://doi.org/10.1029/2007GL030812>.
- , —, and —, 2011: Global observations of nonlinear mesoscale eddies. *Prog. Oceanogr.*, **91**, 167–216, <https://doi.org/10.1016/j.pocean.2011.01.002>.
- Danilov, S., D. Sidorenko, Q. Wang, and T. Jung, 2017: The Finite-Volume Sea Ice–Ocean Model (FESOM2). *Geosci. Model Dev.*, **10**, 765–789, <https://doi.org/10.5194/gmd-10-765-2017>.
- Dmitrenko, I. A., and Coauthors, 2014: Heat loss from the Atlantic Water layer in the northern Kara Sea: Causes and consequences. *Ocean Sci.*, **10**, 719–730, <https://doi.org/10.5194/os-10-719-2014>.
- , and Coauthors, 2015: Atlantic Water flow into the Arctic Ocean through the St. Anna Trough in the northern Kara Sea. *J. Geophys. Res. Oceans*, **120**, 5158–5178, <https://doi.org/10.1002/2015JC010804>.
- Heuzé, C., A. Wählin, H. L. Johnson, and A. Münchow, 2017: Pathways of meltwater export from Petermann Glacier, Greenland. *J. Phys. Oceanogr.*, **47**, 405–418, <https://doi.org/10.1175/JPO-D-16-0161.1>.
- Ivanov, V. V., G. I. Shapiro, J. M. Huthnance, D. L. Aleynik, and P. N. Golovin, 2004: Cascades of dense water around the world ocean. *Prog. Oceanogr.*, **60**, 47–98, <https://doi.org/10.1016/j.pocean.2003.12.002>.
- Jakobsson, M., and Coauthors, 2020: The International Bathymetric Chart of the Arctic Ocean version 4.0. *Sci. Data*, **7**, 176, <https://doi.org/10.1038/s41597-020-0520-9>.
- Jenkins, A., 1999: The impact of melting ice on ocean waters. *J. Phys. Oceanogr.*, **29**, 2370–2381, [https://doi.org/10.1175/1520-0485\(1999\)029<2370:TIOMIO>2.0.CO;2](https://doi.org/10.1175/1520-0485(1999)029<2370:TIOMIO>2.0.CO;2).
- Jones, E. P., B. Rudels, and L. G. Anderson, 1995: Deep waters of the Arctic Ocean: Origins and circulation. *Deep-Sea Res. I*, **42**, 737–760, [https://doi.org/10.1016/0967-0637\(95\)00013-V](https://doi.org/10.1016/0967-0637(95)00013-V).
- Köhl, A., R. H. Käse, D. Stammer, and N. Serra, 2007: Causes of changes in the Denmark Strait overflow. *J. Phys. Oceanogr.*, **37**, 1678–1696, <https://doi.org/10.1175/JPO3080.1>.
- Langehaug, H. R., and E. Falck, 2012: Changes in the properties and distribution of the intermediate and deep waters in the Fram Strait. *Prog. Oceanogr.*, **96**, 57–76, <https://doi.org/10.1016/j.pocean.2011.10.002>.
- Liu, Y., C. Dong, Y. Guan, D. Chen, J. McWilliams, and F. Nencioli, 2012: Eddy analysis in the subtropical zonal band of the North Pacific Ocean. *Deep-Sea Res. I*, **68**, 54–67, <https://doi.org/10.1016/j.dsr.2012.06.001>.
- Mamayev, O. I., 1975: Introduction. *Temperature–Salinity Analysis of World Ocean Waters*, O. I. Mamayev, Ed., Elsevier Oceanography Series, Vol. 11, Elsevier, 1–7, [https://doi.org/10.1016/S0422-9894\(08\)71168-1](https://doi.org/10.1016/S0422-9894(08)71168-1).
- Marnela, M., B. Rudels, I. Goszczko, A. Beszczynska-Möller, and U. Schauer, 2016: Fram Strait and Greenland Sea transports, water masses, and water mass transformations 1999–2010 (and beyond). *J. Geophys. Res. Oceans*, **121**, 2314–2346, <https://doi.org/10.1002/2015JC011312>.
- Mason, E., A. Pascual, and J. C. McWilliams, 2014: A new sea surface height–based code for oceanic mesoscale eddy tracking. *J. Atmos. Oceanic Technol.*, **31**, 1181–1188, <https://doi.org/10.1175/JTECH-D-14-00019.1>.
- McDougall, T. J., and P. M. Barker, 2011: Getting started with TEOS-10 and the Gibbs Seawater (GSW) oceanographic toolbox. Tech Rep. SCOR/IAPSO WG127, 32 pp., [https://www.teos-10.org/pubs/gsw/v3\\_04/pdf/Getting\\_Started.pdf](https://www.teos-10.org/pubs/gsw/v3_04/pdf/Getting_Started.pdf).
- Meneghello, G., J. Marshall, C. Lique, P. E. Isachsen, E. Doddridge, J.-M. Campin, H. Regan, and C. Talandier, 2021: Genesis and decay of mesoscale baroclinic eddies in the seasonally ice-covered interior Arctic Ocean. *J. Phys. Oceanogr.*, **51**, 115–129, <https://doi.org/10.1175/JPO-D-20-0054.1>.
- Muilwijk, M., L. H. Smedsrud, M. Ilicak, and H. Drange, 2018: Atlantic Water heat transport variability in the 20th century Arctic Ocean from a global ocean model and observations. *J. Geophys. Res. Oceans*, **123**, 8159–8179, <https://doi.org/10.1029/2018JC014327>.
- Müller, V., D. Kieke, P. G. Myers, C. Pennelly, and C. Mertens, 2017: Temperature flux carried by individual eddies across 47°N in the Atlantic Ocean. *J. Geophys. Res. Oceans*, **122**, 2441–2464, <https://doi.org/10.1002/2016JC012175>.
- , —, —, —, R. Steinfeldt, and I. Stendardo, 2019: Heat and freshwater transport by mesoscale eddies in the

- southern subpolar North Atlantic. *J. Geophys. Res. Oceans*, **124**, 5565–5585, <https://doi.org/10.1029/2018JC014697>.
- Nansen, F., 1907: Bathymetrical chart of North Polar Seas. Royal Geographic Society, <http://pi.lib.uchicago.edu/1001/cat/bib/7195644>.
- Nencioli, F., C. Dong, T. Dickey, L. Washburn, and J. C. McWilliams, 2010: A vector geometry-based eddy detection algorithm and its application to a high-resolution numerical model product and high-frequency radar surface velocities in the Southern California Bight. *J. Atmos. Oceanic Technol.*, **27**, 564–579, <https://doi.org/10.1175/2009JTECHO725.1>.
- Nixdorf, U., and Coauthors, 2021: MOSAiC extended acknowledgement. Zenodo, <https://doi.org/10.5281/zenodo.5541624>.
- Nurser, A. J. G., and S. Bacon, 2014: The Rossby radius in the Arctic Ocean. *Ocean Sci.*, **10**, 967–975, <https://doi.org/10.5194/os-10-967-2014>.
- Perry, R. K., and Coauthors, 1986: Bathymetry of the Arctic Ocean. Geological Society of America Map and Chart Series, MC-56, Boulder, Colorado, scale 1:4,704,075, [https://www.gebco.net/about\\_us/committees\\_and\\_groups/scrumb/ibcao/documents/ibcaoposter.pdf](https://www.gebco.net/about_us/committees_and_groups/scrumb/ibcao/documents/ibcaoposter.pdf).
- Pnyushkov, A., I. V. Polyakov, L. Padman, and A. T. Nguyen, 2018: Structure and dynamics of mesoscale eddies over the Laptev Sea continental slope in the Arctic Ocean. *Ocean Sci.*, **14**, 1329–1347, <https://doi.org/10.5194/os-14-1329-2018>.
- Polyakov, I. V., L. Padman, Y.-D. Lenn, A. Pnyushkov, R. Rember, and V. V. Ivanov, 2019: Eastern Arctic Ocean diapycnal heat fluxes through large double-diffusive steps. *J. Phys. Oceanogr.*, **49**, 227–246, <https://doi.org/10.1175/JPO-D-18-0080.1>.
- Rabe, B., and Coauthors, 2022: Overview of the MOSAiC expedition: Physical oceanography. *Elementa*, **10**, 00062, <https://doi.org/10.1525/elementa.2021.00062>.
- Rudels, B., 1986: The  $\theta$ -S relations in the northern seas: Implications for the deep circulation. *Polar Res.*, **4**, 133–159, <https://doi.org/10.3402/polar.v4i2.6928>.
- , 1995: The thermohaline circulation of the Arctic Ocean and the Greenland Sea. *Philos. Trans. Roy. Soc.*, **A352**, 287–299, <https://doi.org/10.1098/rsta.1995.0071>.
- , 2012: Arctic Ocean circulation and variability—Advection and external forcing encounter constraints and local processes. *Ocean Sci.*, **8**, 261–286, <https://doi.org/10.5194/os-8-261-2012>.
- , 2021: *The Physical Oceanography of the Arctic Mediterranean Sea: Explorations, Observations, Interpretations*. Elsevier, 536 pp.
- , R. D. Muench, J. Gunn, U. Schauer, and H. J. Friedrich, 2000: Evolution of the Arctic Ocean boundary current north of the Siberian shelves. *J. Mar. Syst.*, **25**, 77–99, [https://doi.org/10.1016/S0924-7963\(00\)00009-9](https://doi.org/10.1016/S0924-7963(00)00009-9).
- , E. Fahrbach, J. Meincke, G. Budéus, and P. Eriksson, 2002: The East Greenland Current and its contribution to the Denmark Strait overflow. *ICES J. Mar. Sci.*, **59**, 1133–1154, <https://doi.org/10.1006/jmsc.2002.1284>.
- , U. Schauer, G. Björk, M. Korhonen, S. Pisarev, B. Rabe, and A. Wisotzki, 2013: Observations of water masses and circulation with focus on the Eurasian Basin of the Arctic Ocean from the 1990s to the late 2000s. *Ocean Sci.*, **9**, 147–169, <https://doi.org/10.5194/os-9-147-2013>.
- Schauer, U., and Coauthors, 2002: Confluence and redistribution of Atlantic Water in the Nansen, Amundsen and Makarov Basins. *Ann. Geophys.*, **20**, 257–273, <https://doi.org/10.5194/angeo-20-257-2002>.
- Schlosser, P., and Coauthors, 1997: The first trans-Arctic  $^{14}\text{C}$  section: Comparison of the mean ages of the deep waters in the Eurasian and Canadian Basins of the Arctic Ocean. *Nucl. Instrum. Methods Phys. Res., Sect. B*, **123**, 431–437, [https://doi.org/10.1016/S0168-583X\(96\)00677-5](https://doi.org/10.1016/S0168-583X(96)00677-5).
- Schulz, K., V. Mohrholz, I. Fer, M. Janout, M. Hoppmann, J. Schaffer, and Z. Koenig, 2022: A full year of turbulence measurements from a drift campaign in the Arctic Ocean 2019–2020. *Sci. Data*, **9**, 472, <https://doi.org/10.1038/s41597-022-01574-1>.
- Shibley, N. C., M.-L. Timmermans, J. R. Carpenter, and J. M. Toole, 2017: Spatial variability of the Arctic Ocean's double-diffusive staircase. *J. Geophys. Res. Oceans*, **122**, 980–994, <https://doi.org/10.1002/2016JC012419>.
- Snoeijs-Leijonmalm, P., 2022: *Expedition Report SWEDARCTIC: Synoptic Arctic Survey 2021 with Icebreaker Oden*. 1st ed. Swedish Polar Research Secretariat, 310 pp.
- Somavilla, R., U. Schauer, and G. Budéus, 2013: Increasing amount of Arctic Ocean deep waters in the Greenland Sea. *Geophys. Res. Lett.*, **40**, 4361–4366, <https://doi.org/10.1002/grl.50775>.
- Steele, M., R. Morley, and W. Ermold, 2001: PHC: A global ocean hydrography with a high-quality Arctic Ocean. *J. Climate*, **14**, 2079–2087, [https://doi.org/10.1175/1520-0442\(2001\)014<2079:PAGOHW>2.0.CO;2](https://doi.org/10.1175/1520-0442(2001)014<2079:PAGOHW>2.0.CO;2).
- Swift, J. H., E. P. Jones, K. Aagaard, E. C. Carmack, M. Hingston, R. W. Macdonald, F. A. McLaughlin, and R. G. Perkin, 1997: Waters of the Makarov and Canada Basins. *Deep-Sea Res. II*, **44**, 1503–1529, [https://doi.org/10.1016/S0967-0645\(97\)00055-6](https://doi.org/10.1016/S0967-0645(97)00055-6).
- Tanhua, T., E. P. Jones, E. Jeansson, S. Jutterström, W. M. Smethie Jr., D. W. R. Wallace, and L. G. Anderson, 2009: Ventilation of the Arctic Ocean: Mean ages and inventories of anthropogenic  $\text{CO}_2$  and CFC-11. *J. Geophys. Res.*, **114**, C01002, <https://doi.org/10.1029/2008JC004868>.
- Timmermans, M.-L., and C. Garrett, 2006: Evolution of the deep water in the Canadian Basin in the Arctic Ocean. *J. Phys. Oceanogr.*, **36**, 866–874, <https://doi.org/10.1175/JPO2906.1>.
- , and J. Marshall, 2020: Understanding Arctic Ocean circulation: A review of ocean dynamics in a changing climate. *J. Geophys. Res. Oceans*, **125**, e2018JC014378, <https://doi.org/10.1029/2018JC014378>.
- , C. Garrett, and E. Carmack, 2003: The thermohaline structure and evolution of the deep waters in the Canada Basin, Arctic Ocean. *Deep-Sea Res. I*, **50**, 1305–1321, [https://doi.org/10.1016/S0967-0637\(03\)00125-0](https://doi.org/10.1016/S0967-0637(03)00125-0).
- , P. Winsor, and J. A. Whitehead, 2005: Deep-water flow over the Lomonosov Ridge in the Arctic Ocean. *J. Phys. Oceanogr.*, **35**, 1489–1493, <https://doi.org/10.1175/JPO2765.1>.
- Tsubouchi, T., K. Våge, B. Hansen, K. M. H. Larsen, S. Østerhus, C. Johnson, S. Jónsson, and H. Valdimarsson, 2021: Increased ocean heat transport into the Nordic Seas and Arctic Ocean over the period 1993–2016. *Nat. Climate Change*, **11**, 21–26, <https://doi.org/10.1038/s41558-020-00941-3>.
- Tsujino, H., and Coauthors, 2018: JRA-55 based surface dataset for driving ocean–sea-ice models (JRA55-do). *Ocean Modell.*, **130**, 79–139, <https://doi.org/10.1016/j.ocemod.2018.07.002>.
- Vlasenko, V., and N. Stashchuk, 2018: Tidally induced overflow of the Faroese Channels bottom water over the Wyville Thomson Ridge. *J. Geophys. Res. Oceans*, **123**, 6753–6765, <https://doi.org/10.1029/2018JC014365>.
- von Appen, W.-J., U. Schauer, R. Somavilla, E. Bauerfeind, and A. Beszczynska-Möller, 2015: Exchange of warming deep waters across Fram Strait. *Deep-Sea Res. I*, **103**, 86–100, <https://doi.org/10.1016/j.dsr.2015.06.003>.
- Walczowski, W., J. Piechura, I. Goszczko, and P. Wiczorek, 2012: Changes in Atlantic Water properties: An important factor in

- the European Arctic marine climate. *ICES J. Mar. Sci.*, **69**, 864–869, <https://doi.org/10.1093/icesjms/fss068>.
- Wang, Q., N. V. Koldunov, S. Danilov, D. Sidorenko, C. Wekerle, P. Scholz, I. L. Bashmachnikov, and T. Jung, 2020: Eddy kinetic energy in the Arctic Ocean from a global simulation with a 1-km Arctic. *Geophys. Res. Lett.*, **47**, e2020GL088550, <https://doi.org/10.1029/2020GL088550>.
- Wekerle, C., T. Hattermann, Q. Wang, L. Crews, W.-J. von Appen, and S. Danilov, 2020: Properties and dynamics of mesoscale eddies in Fram Strait from a comparison between two high-resolution ocean–sea ice models. *Ocean Sci.*, **16**, 1225–1246, <https://doi.org/10.5194/os-16-1225-2020>.
- Woodgate, R. A., K. Aagaard, R. D. Muench, J. Gunn, G. Björk, B. Rudels, A. T. Roach, and U. Schauer, 2001: The Arctic Ocean boundary current along the Eurasian slope and the adjacent Lomonosov Ridge: Water mass properties, transports and transformations from moored instruments. *Deep-Sea Res. I*, **48**, 1757–1792, [https://doi.org/10.1016/S0967-0637\(00\)00091-1](https://doi.org/10.1016/S0967-0637(00)00091-1).
- Zhao, M., and M.-L. Timmermans, 2015: Vertical scales and dynamics of eddies in the Arctic Ocean’s Canada Basin. *J. Geophys. Res. Oceans*, **120**, 8195–8209, <https://doi.org/10.1002/2015JC011251>.
- , —, S. Cole, R. Krishfield, A. Proshutinsky, and J. Toole, 2014: Characterizing the eddy field in the Arctic Ocean halocline. *J. Geophys. Res. Oceans*, **119**, 8800–8817, <https://doi.org/10.1002/2014JC010488>.
- Zheng, Y., K. J. Heywood, B. G. M. Webber, D. P. Stevens, L. C. Biddle, L. Boehme, and B. Loose, 2021: Winter seal-based observations reveal glacial meltwater surfacing in the southeastern Amundsen Sea. *Commun. Earth Environ.*, **2**, 40, <https://doi.org/10.1038/s43247-021-00111-z>.